



# ATLAS NOTE

## ATLAS-CONF-2012-046

May 14, 2012



### Search for physics beyond the Standard Model in events with a $Z$ boson and large missing transverse momentum with the ATLAS detector

The ATLAS Collaboration

#### Abstract

This note presents a search for supersymmetry in the final state defined by a  $Z$  boson and missing transverse momentum. The analysis uses a data sample collected during the first half of 2011 that corresponds to a total integrated luminosity of  $1.04 \text{ fb}^{-1}$  of  $\sqrt{s} = 7 \text{ TeV}$  proton-proton collisions recorded with the ATLAS detector at the Large Hadron Collider. No excess above the Standard Model background expectation is observed. The results are interpreted in the context of a general gauge mediation (GGM) scenario, where the lightest neutralino, which is the next-to-lightest supersymmetric particle, is higgsino-like. For higgsino masses in the range  $200 - 640 \text{ GeV}$ , gluino masses up to  $600 - 700 \text{ GeV}$  are excluded at 95% CL.

# 1 Introduction

Supersymmetry (SUSY) [1–9] is one of the most popular extensions of the Standard Model (SM) that provides solutions to some of its shortcomings. SUSY transformations turn bosonic states into fermionic states, and vice versa. The minimal supersymmetric extension to the SM (MSSM) [10–14] predicts a supersymmetric partner (or superpartner) for each SM particle, that differs in spin by 1/2 from its SM counterpart. In  $R$ -parity conserving SUSY [10–14], each supersymmetric interaction involves an even number of sparticles, and as a result there exists a lightest supersymmetric particle (LSP) that must be stable. In many SUSY models, the LSP serves as a viable candidate for non-baryonic dark matter. Assuming  $R$ -parity conservation, SUSY production is characterized by pair-produced sparticles, which then decay via long chains, otherwise known as “cascades”, into final states involving LSPs.

Because evidence for supersymmetric particles has not yet been found, if SUSY exists, it must be a broken symmetry, allowing the superpartners to be heavier than the corresponding SM particles. One popular scenario that provides a formalism to explain the mechanism of SUSY breaking, which in turn gives rise to the superpartner masses and interactions, is gauge-mediated supersymmetry breaking (GMSB). In GMSB models [15–20], SUSY is broken in a hidden sector and the SUSY breaking is propagated to the visible sector via SM-like  $S U(3)_C \times S U(2)_L \times U(1)_Y$  gauge boson and gaugino interactions of some new chiral supermultiplets, called messengers, and the MSSM particles. The main advantage of GMSB models relative to the minimal supergravity and anomaly mediated SUSY breaking models is that scalars with the same gauge quantum numbers, but different flavors, have identical soft SUSY breaking masses. As a result, flavor-changing neutral currents (FCNC) are suppressed.

In GMSB, the gravitino ( $\tilde{G}$ ) is the LSP (in general  $m(\tilde{G}) \ll 1$  keV). The gravitino escapes detection, leading to missing transverse momentum (denoted  $\mathbf{p}_T^{\text{miss}}$  and its magnitude  $E_T^{\text{miss}}$ ). The phenomenology of GMSB models is determined by the nature of the next-to-lightest supersymmetric particle (NLSP), which for a large part of the GMSB parameter space is the lightest neutralino  $\tilde{\chi}_1^0$ .

Neutralinos are mixtures of gaugino ( $\tilde{B}$ ,  $\tilde{W}^0$ ) and higgsino ( $\tilde{H}_u^0$ ,  $\tilde{H}_d^0$ ) eigenstates, and therefore the lightest neutralino decays to a  $\tilde{G}$  and either a  $\gamma$ ,  $Z$ , or Higgs boson ( $H$ ). If the  $\tilde{\chi}_1^0$  is bino-like, the main decay mode is  $\tilde{\chi}_1^0 \rightarrow \gamma \tilde{G}$ . If the  $\tilde{\chi}_1^0$  is higgsino-like, it decays as  $\tilde{\chi}_1^0 \rightarrow H \tilde{G}$ . In addition, since the longitudinal polarization component of the  $Z$  boson is also a Goldstone mode of the Higgs field, a higgsino-like neutralino can also decay as  $\tilde{\chi}_1^0 \rightarrow Z \tilde{G}$ . Consequently, a pair of  $\tilde{\chi}_1^0$ s produced in a collider can give rise to the diboson final states ( $HH$ ,  $H\gamma$ ,  $HZ$ ,  $Z\gamma$ ,  $ZZ$ ,  $\gamma\gamma$ ) +  $E_T^{\text{miss}}$ . The  $Z$ -rich case of higgsino-like neutralino NLSPs, where  $BR(\tilde{\chi}_1^0 \rightarrow H \tilde{G})$  is negligible, is considered in this paper. In this scenario both neutralinos decay as  $\tilde{\chi}_1^0 \rightarrow Z \tilde{G}$ , leading to the final state  $ZZ + E_T^{\text{miss}}$ . Due to the low branching ratio of  $Z$  to leptons, the four lepton final state has a low acceptance times branching ratio. Therefore, the final state that includes at least one  $Z$  boson which decays to a pair of electrons or muons is considered here.

Searches for GMSB at the Tevatron were interpreted in a simplified GMSB scenario using a minimal GMSB model, where the  $\tilde{\chi}_1^0$  is bino-like [21, 22]. In recent years, the effort to formulate GMSB in a model-independent way has led to the development of general gauge mediation (GGM) [23, 24]. GGM includes an observable sector with all the MSSM fields, together with a hidden sector that contains the source of SUSY breaking. In GGM, there need not be any hierarchy between colored and uncolored states, and thus there is no theoretical constraint on how light the colored states can be. Removing this constraint raises the probability of GGM discovery even with early LHC data. Both ATLAS and CMS have performed searches for GGM models with bino-like  $\tilde{\chi}_1^0$ s [25, 26]. CMS also performed a search for wino-like  $\tilde{\chi}_1^0$  GGM [27]. No excesses above the SM background expectations were observed.

In the GGM SUSY models considered in this analysis and suggested in [28, 29], the gluino mass ( $m(\tilde{g})$ ) and the higgsino mass parameter ( $m(\tilde{H})$ ) are treated as free parameters. All other sparticle masses are fixed at  $\sim 1.5$  TeV, which leads to gluino pair production via strong interactions being the dominant production mode. The gluinos then cascade-decay into final states involving the NLSP  $\tilde{\chi}_1^0$  and jets. The

$U(1)$  and  $SU(2)$  gaugino mass parameters ( $M_1$  and  $M_2$ ) are fixed to 1 TeV. In this particular region of parameter space, the two lightest neutralinos ( $\tilde{\chi}_1^0$  and  $\tilde{\chi}_2^0$ ) and lightest chargino ( $\tilde{\chi}_1^\pm$ ) become higgsino-like. In the limit  $(M_1, M_2) \rightarrow \infty$ , the exact relations  $m(\tilde{\chi}_1^0) = m(\tilde{\chi}_2^0) = m(\tilde{\chi}_1^\pm) = m(\tilde{H})$  hold true. In practice,  $M_1$  and  $M_2$  are never infinite, and therefore the effect of neutralino and chargino mixing will push the masses of  $\tilde{\chi}_1^0$ ,  $\tilde{\chi}_2^0$  and  $\tilde{\chi}_1^\pm$  away from  $m(\tilde{H})$ . A  $\tan\beta$  value of 1.5 was chosen to ensure  $\tilde{\chi}_1^0 \rightarrow Z\tilde{G}$  is the dominant NLSP decay ( $BR(\tilde{\chi}_1^0 \rightarrow Z\tilde{G}) \sim 97\%$ ) [28]. Finally, the NLSP decay length is fixed to be  $c\tau_{\text{NLSP}} < 0.1$  mm.

The three-body gluino decays  $\tilde{g} \rightarrow q\bar{q}\tilde{\chi}_1^0$  and  $\tilde{g} \rightarrow q\bar{q}\tilde{\chi}_2^0$  followed by the higgsino-like  $\tilde{\chi}_2^0$  decay  $\tilde{\chi}_2^0 \rightarrow \tilde{\chi}_1^0 f\bar{f}$  and  $\tilde{\chi}_1^0$  decay  $\tilde{\chi}_1^0 \rightarrow Z\tilde{G}$  are expected to lead to final states that are characterised by the presence of at least one  $Z$  boson, which decays to a pair of electrons or muons, and large  $E_T^{\text{miss}}$ . The  $E_T^{\text{miss}}$  results from the undetected gravitinos. The main SM backgrounds are the  $Z/\gamma^* + \text{jets}$ ,  $t\bar{t}$ , single-top, and diboson processes. The evaluation of the instrumental  $Z/\gamma^* + \text{jets}$  background, which has  $E_T^{\text{miss}}$  that is mostly due to hadronic mismeasurement, was made using a sample of  $\gamma + \text{jets}$  events. The top quark and diboson backgrounds were estimated using Monte Carlo (MC) simulation.

## 2 ATLAS detector

The ATLAS detector [30] is a general-purpose particle detector with forward-backward symmetric cylindrical geometry. ATLAS consists of inner tracking devices surrounded by a superconducting solenoid, electromagnetic and hadronic calorimeters, and a muon spectrometer with a toroidal magnetic field. The inner detector (ID) consists of a silicon pixel detector, a silicon microstrip detector (SCT), and a transition radiation tracker (TRT). In combination with the 2 T field from the solenoid, the ID provides precision tracking of charged particles for  $|\eta| < 2.5$ <sup>1</sup>. The calorimeter system covers the pseudorapidity range  $|\eta| < 4.9$  and is composed of sampling calorimeters with either liquid argon (LAr) or scintillating tiles as the active media. The muon spectrometer has separate trigger and high precision tracking chambers which provide muon identification and measurement for  $|\eta| < 2.7$ .

## 3 Simulation

Simulated MC event samples were used to model the SUSY signal and to describe the SM background.

For the GGM models, the SUSY mass spectra, the gluino branching ratios, and the gluino decay width were calculated using SUSPECT 2.41 [31] and SDECAY 1.3 [32]. The MC signal samples were generated using PYTHIA 6.423 [33] with MRST2007 LO\* [34] parton distribution functions (PDF). The next-to-leading order (NLO) production cross-sections for the SUSY signal points were calculated using PROSPINO 2.1 [35] with the CTEQ6.6M [36] PDF set.

Single-top and  $t\bar{t}$  production were simulated using MC@NLO [37] with the NLO PDF set CTEQ6.6 [38]. POWHEG [39] samples were used to assess the systematic uncertainties associated with the choice of generator for  $t\bar{t}$  production. ACERMC [40] samples were used to assess the uncertainties associated with initial and final state radiation (ISR/FSR). The  $Z/\gamma^* + \text{jets}$  and  $W + \text{jets}$  samples were generated using ALPGEN [41] with PDF set CTEQ6L1 [42] and normalized to inclusive next-to-next-to-leading (NNLO) cross-sections. Parton showering and fragmentation were simulated by the HERWIG [43] generator with JIMMY [44] generating the underlying event. Diboson ( $ZZ$ ,  $WZ$  and  $WW$ ) samples were generated with HERWIG and normalized to NLO cross-sections.

<sup>1</sup>ATLAS uses a right-handed coordinate system with its origin at the nominal interaction point in the centre of the detector and the  $z$ -axis coinciding with the axis of the beam pipe. The  $x$ -axis points from the IP to the center of the LHC ring, and the  $y$ -axis points upward. Cylindrical coordinates  $(r, \phi)$  are used in the transverse plane,  $\phi$  being the azimuthal angle around the beam pipe. The pseudorapidity is defined in terms of the polar angle  $\theta$  as  $\eta = -\ln \tan(\theta/2)$ . The distance  $\Delta R$  in the  $\eta - \phi$  space is defined as  $\Delta R = \sqrt{(\Delta\eta)^2 + (\Delta\phi)^2}$ .

All samples were processed through the GEANT4 simulation [45, 46] of the ATLAS detector [30]. The in-time and out-of-time pile-up conditions, which result from multiple proton-proton interactions per crossing, were taken into account by overlaying minimum-bias events on the hard-scattering process in each MC sample. The simulated events were then reweighted such that the distribution of the number of interactions per crossing in MC matched the one observed in data.

## 4 Object and Event Selection

The analysis is performed using data recorded in proton-proton collisions at a center-of-mass energy of 7 TeV, corresponding to an integrated luminosity of  $\int \mathcal{L} dt = 1.04 \pm 0.04 \text{ fb}^{-1}$  [47] after the application of beam, detector and data quality requirements. Events are selected using single electron and muon triggers that have constant efficiency as a function of lepton transverse momentum ( $p_T$ ) above the offline  $p_T$  cuts used in the analysis. The photon data sample, required for the evaluation of the instrumental  $Z/\gamma^* + \text{jets}$  background, is collected using a single photon trigger that selects a stream of photon events using a  $p_T$  threshold of 40 GeV. This photon trigger, which is prescaled to maintain reasonable trigger rates during data taking, selects a data sample corresponding to an integrated luminosity of  $\int \mathcal{L} dt = 80.8 \pm 3.0 \text{ pb}^{-1}$ .

Jets are reconstructed using the anti- $k_t$  jet clustering algorithm [48] with a distance parameter of  $R = 0.4$  (in  $y - \phi$  space). Jets are required to have  $p_T > 20 \text{ GeV}$  and lie within  $|\eta| < 2.8$ . Electron candidates are required to have  $p_T > 20 \text{ GeV}$  and  $|\eta| < 2.47$  and pass the “medium” shower shape and track selection criteria [49]. Muon candidates within  $|\eta| < 2.4$  are considered, and their  $p_T$  must be greater than 10 GeV. Muons are identified by matching an extrapolated inner detector track and one or more track segments in the muon spectrometer [50]. The leading lepton is required to have  $p_T > 25 \text{ GeV}$  if it is an electron and  $p_T > 20 \text{ GeV}$  if it is a muon. Photon candidates are required to have  $p_T > 45 \text{ GeV}$  and  $|\eta| < 1.81$ , removing  $|\eta| \in [1.37, 1.52]$ , and must satisfy the “tight” selection criteria [51]. To avoid overlap, any electron within  $\Delta R < 0.01$  of a selected photon is discarded. In addition, any jet within  $\Delta R < 0.2$  of any remaining electron is removed. Finally, electron or muon candidates within  $\Delta R < 0.4$  of any remaining jet are also discarded. The missing transverse momentum is calculated from the energy deposited in calorimeter cells inside three-dimensional clusters with  $|\eta| < 4.9$  and is corrected for contributions from muons, if any [52]. The cluster energy is calibrated to correct for the non-compensating calorimeter response, energy loss in dead material, and out-of-cluster energy.

After performing the baseline object selection described above, including jet overlap removal, electron candidates must pass the “tight” selection criteria [49], which adds a requirement on the ratio  $E/p$ , where  $E$  is the calorimeter cluster energy and  $p$  is the track momentum, and the detection of transition radiation. Furthermore, an isolation requirement is imposed by requiring that the sum of the  $p_T$  of tracks within  $\Delta R < 0.2$  around an electron candidate must be less than 10% of the electron  $p_T$ . Muon candidates must have longitudinal and transverse impact parameter values within 1 mm and 0.2 mm of the primary vertex, respectively, and are required to be isolated. The isolation requirement is that the sum of the  $p_T$  of tracks within  $\Delta R < 0.2$  around a muon candidate is less than 1.8 GeV.

Events that contain at least two muons or electrons with opposite charge with an invariant mass in a window around the  $Z$  boson mass, [81, 101] GeV, are selected.

When plotting kinematic distributions of the  $Z$ -selected events, two representative GGM signal points, which are characterised by the  $gg \rightarrow \tilde{g}\tilde{g}$  production mechanism, are chosen to illustrate the SUSY contribution:

- $m(\tilde{g}) = 300 \text{ GeV}, m(\tilde{H}) = 120 \text{ GeV}$  represents the region  $m(\tilde{g}) > m(\tilde{H})$ .
- $m(\tilde{g}) = 300 \text{ GeV}, m(\tilde{H}) = 290 \text{ GeV}$  represents the region  $m(\tilde{g}) \approx m(\tilde{H})$ .

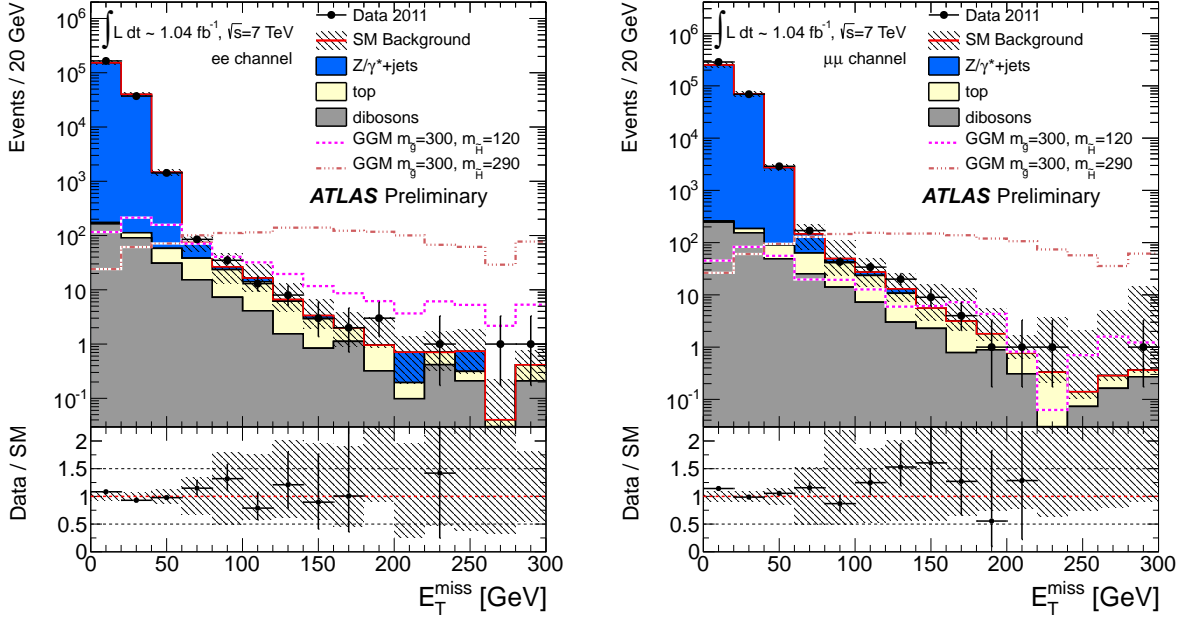


Figure 1: Distribution of  $E_T^{\text{miss}}$  for data and MC events after  $Z \rightarrow e^\pm e^\mp$  (left) and  $Z \rightarrow \mu^\pm \mu^\mp$  (right) selections. Two GGM signal points are included. The first point was produced with  $m(\tilde{q}) = 300$  GeV and  $m(\tilde{H}) = 120$  GeV, and the second with  $m(\tilde{q}) = 300$  GeV and  $m(\tilde{H}) = 290$  GeV. The plot labeled “Data/SM” shows the ratio of the distribution from data to that of the total SM background. The error bars on the data represent statistical uncertainties. The hatched grey band represents the systematic uncertainties on the MC expectation without uncertainties on the  $t\bar{t}$  generator and ISR/FSR effects. The plots include the overflow bin.

By examining these GGM grid points, one can see how the SUSY contributions from different kinematic regions behave in the distributions of interest. The source of the  $E_T^{\text{miss}}$  in the GGM models is the  $\tilde{G}$ , which is produced in the decay  $\tilde{\chi}_1^0 \rightarrow Z\tilde{G}$ . As a result,  $E_T^{\text{miss}}$  depends on  $m(\tilde{H})$ . This can be seen in Figure 1, which shows the  $E_T^{\text{miss}}$  distribution of data and MC events after the  $Z$  mass requirement for the  $ee$  and  $\mu\mu$  channels.

Due to the different kinematics of the GGM signal points, two signal regions were selected to optimize the GGM search throughout the parameter space. The signal regions, characterised by  $E_T^{\text{miss}}$ , jet multiplicity, and the scalar sum of the  $p_T$  of all reconstructed objects (denoted  $H_T \equiv \sum_i p_T^{\text{jet},i} + \sum_i p_T^{\text{lepton},i} + \sum_i p_T^{\text{photon},i}$ ) are defined as shown in Table 1. The cut on  $p_T(Z)$  was motivated by the trigger  $p_T$  threshold for the photon data sample used in the evaluation of the  $Z/\gamma^* + \text{jets}$  background. The decrease in the acceptance of the signal MC due to this cut is negligible. The  $H_T$  distributions of data and MC events after the  $Z$  mass requirement for the  $ee$  and  $\mu\mu$  channels are shown in Figure 2. This variable is used in the signal region definitions to select events with high levels of hadronic activity.

## 5 Background Evaluation

A data-driven method for the instrumental  $Z/\gamma^* + \text{jets}$  background evaluation was developed for this analysis. The  $t\bar{t}$ , single-top, and diboson contributions were estimated using MC.

After the  $Z$  mass requirement, one of the dominant SM backgrounds is  $Z/\gamma^* + \text{jets}$ . Since only  $Z \rightarrow ee$  and  $Z \rightarrow \mu\mu$  (and not  $Z \rightarrow \tau\tau$ ) decays were selected, this background has  $E_T^{\text{miss}}$  that mostly stems from mismeasurement of the reconstructed objects, especially jets. To estimate the contribution of

Signal Region	SR1	SR2
$E_T^{\text{miss}} [\text{GeV}]$	>220	>140
Leading jet $p_T [\text{GeV}]$	>80	-
Second jet $p_T [\text{GeV}]$	>40	-
Third jet $p_T [\text{GeV}]$	>40	-
$H_T [\text{GeV}]$	-	>300
$p_T(Z) [\text{GeV}]$	>45	>45

Table 1: Criteria for each of the signal regions.

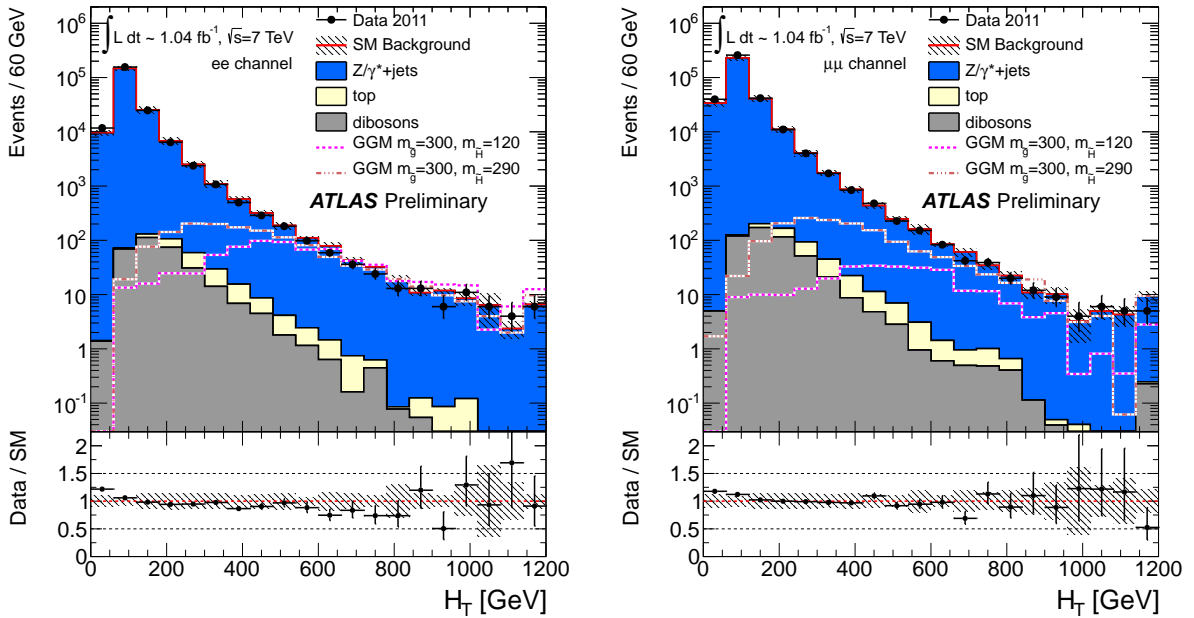


Figure 2: Distributions of  $H_T$  for data and MC events after  $Z \rightarrow e^\pm e^\mp$  (left) and  $Z \rightarrow \mu^\pm \mu^\mp$  (right) selections. Two GGM signal points are included. The first point was produced with  $m(\tilde{g}) = 300$  GeV and  $m(\tilde{H}) = 120$  GeV, and the second with  $m(\tilde{g}) = 300$  GeV and  $m(\tilde{H}) = 290$  GeV. The hatched grey band represents the systematic uncertainties on the MC expectations without uncertainties on the  $t\bar{t}$  generator and ISR/FSR effects. The plots include the overflow bin.

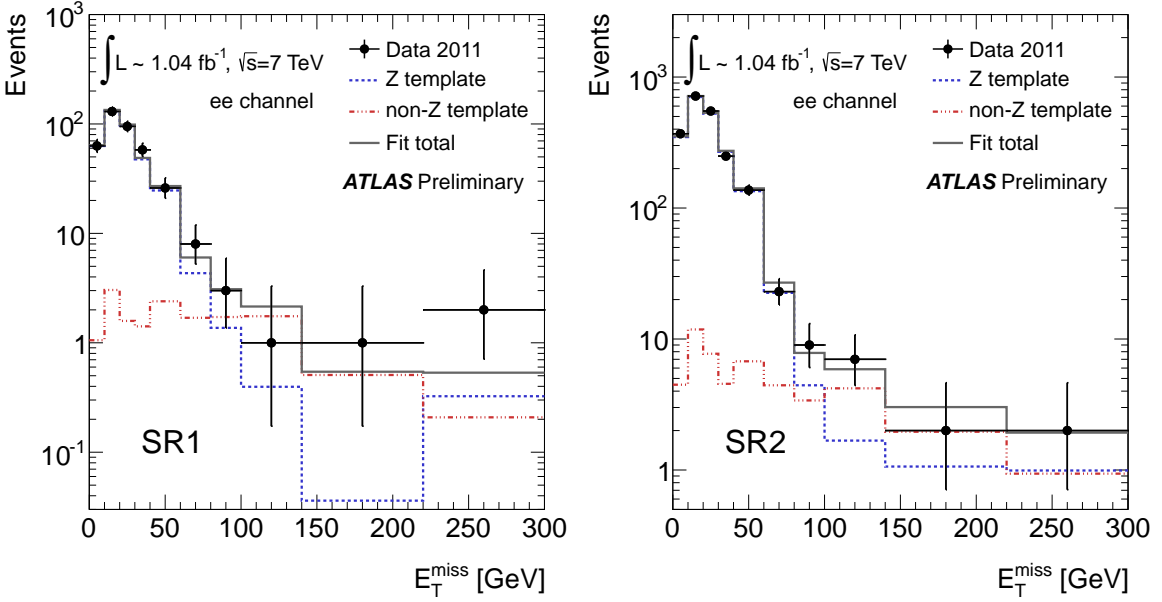


Figure 3: Distributions of the  $E_T^{\text{miss}}$  for data events after SR1 (left) and SR2 (right) selection without the  $E_T^{\text{miss}}$  requirement for the  $ee$  channel. The  $\gamma + \text{jets}$  template for  $Z/\gamma^* + \text{jets}$  and the non- $Z$  MC distribution of  $E_T^{\text{miss}}$ , which serves as the template for non- $Z$  sources, are shown on the plots.

the instrumental  $Z/\gamma^* + \text{jets}$  background in the signal regions, a data control sample of  $\gamma + \text{jets}$  events, which are also characterised by  $E_T^{\text{miss}}$  due to hadronic mismeasurement, was used.

The expected contamination of the photon sample from  $W + \text{jets}$ , top, and diboson processes, which have real  $E_T^{\text{miss}}$  and can be selected if an electron is misidentified as a photon, was evaluated based on a data-driven estimation of the electron-photon fake probability. This probability, as derived in [25], varies between 5% and 17% as a function of  $\eta$ , due to the distribution of material in front of the calorimeter. To evaluate the contamination, the fake probability was applied to reconstructed electrons in MC events, which were then subtracted from the photon sample. The full difference between the contamination found using the data-driven fake probabilities and that based on simulated fake probabilities is assigned as a systematic uncertainty. The contributions from  $W\gamma$  and  $Z\gamma$  processes to the selected photon events were found to be negligible. Contamination from multijet events was found to be small. A systematic uncertainty was applied to account for this contamination.

The expected difference between the  $E_T^{\text{miss}}$  distributions of the photon and  $Z$  samples was corrected by reweighting the background subtracted photon sample, in events with  $E_T^{\text{miss}} < 30$  GeV, such that its  $H_T$  distribution matches that of the  $Z$  data sample. Reweighting was then applied to photon events across the whole  $E_T^{\text{miss}}$  spectrum.

A template method was utilised to evaluate the  $Z/\gamma^* + \text{jets}$  background. The  $Z/\gamma^* + \text{jets}$   $E_T^{\text{miss}}$  template derived from  $\gamma + \text{jets}$  events was fit to data in each signal region over the range  $0 < E_T^{\text{miss}} < 140$  GeV taking the non- $Z$  background component from MC simulation.

The results of the template fits for the estimate in SR1 and SR2 are shown for the electron channel in Figure 3. The estimated  $Z$  and non- $Z$  backgrounds, after applying all the signal regions requirements, are summarized in Section 7.

Signal Region	SR1		SR2	
	$ee$	$\mu\mu$	$ee$	$\mu\mu$
<b>Z background</b>				
Control region definition	64%	21%	21%	12%
MC electron-photon fake probability	10%	21%	38%	39%
Total	65%	33%	46%	44%
<b>non-Z background</b>				
JES	56%	39%	22%	20%
$E_T^{\text{miss}}$	56%	72%	18%	20%
ISR/FSR	20%	38%	15%	18%
Total	85%	93%	33%	35%

Table 2: Fractional values of the dominant and total systematic uncertainties on SM Z and non-Z events for the electron and muon channels in the two SRs.

## 6 Systematic Uncertainties

Systematic uncertainties affecting the background rate and SUSY signal yields in the signal regions have been evaluated. Table 2 summarizes the dominant and total systematic uncertainties on the SM Z and non-Z backgrounds.

The systematic uncertainties on the data-driven estimates of the  $Z/\gamma^* + \text{jets}$  background are found to be 65% (33%) for SR1 and 46% (44%) for SR2 for the electron (muon) channel. The primary sources of this systematic uncertainty are the choice of control region used to derive the  $H_T$  reweighting and the use of different subtraction methods to correct the selected  $\gamma + \text{jets}$  control sample. The large difference between the systematic uncertainties in electron and muon channels in SR1 is due to the stringent SR1 requirements, which lead to statistical fluctuations.

The background from  $t\bar{t}$ , single-top and dibosons is obtained using MC. The total uncertainty on these predictions is estimated to be 85% (93%) for SR1 and 33% (35%) for SR2 for the electron (muon) channel. The uncertainties are dominated by the uncertainty on the jet energy scale, uncertainties associated with ISR and FSR, and the uncertainties in energy scale associated to the calorimeter clusters that are used in the  $E_T^{\text{miss}}$  computation, but which are not associated to any hard objects in the event.

For the SUSY signal processes, various sources of uncertainties affect the theoretical NLO cross-sections. Variations of the renormalisation and factorisation scales by factors of two in the NLO PROSPINO calculation result in uncertainties up to 20%. The PDF uncertainties on the GGM cross-sections were evaluated by using the CTEQ6.6M [36] PDF error sets in the PROSPINO 2.1 [35] cross-section calculation and range from 12% to 29%, depending on the gluino and higgsino masses. The difference in the impact of the PDF and scale uncertainties on the various GGM points is related to the different production mechanisms in the GGM grid considered here. The systematic uncertainties due to experimental sources were also assessed for signal MC and were found to vary from 5–60% for points with large  $m(\tilde{H})$ .

## 7 Results and Interpretation

Table 3 shows the number of expected events in the SRs for each background source together with the observed number of events. In both signal regions, the contribution from QCD and  $W + \text{jets}$  are negligible, and the dominant backgrounds are  $Z/\gamma^* + \text{jets}$  and  $t\bar{t}$ . Due to the jet requirement in SR1, the diboson contribution is negligible.

In Figures 4 and 5 the distributions of  $E_T^{\text{miss}}$  for data and MC events in the  $ee$  and  $\mu\mu$  channels after application of the SR1 and SR2 requirements, except for the  $E_T^{\text{miss}}$  cut, are shown.

Background source	SR1		SR2	
	$ee$	$\mu\mu$	$ee$	$\mu\mu$
top	$0.2 \pm 0.2$	$0.2 \pm 0.1$	$2.2 \pm 1.0$	$3.0 \pm 1.3$
dibosons	-	$0.0 \pm 0.1$	$0.8 \pm 0.2$	$0.9 \pm 0.4$
$Z/\gamma^* + \text{jets}$	$0.3 \pm 0.4$	$0.3 \pm 0.3$	$2.1 \pm 1.2$	$3.2 \pm 1.8$
Total SM Background	$0.5 \pm 0.4$	$0.4 \pm 0.3$	$5.2 \pm 1.7$	$7.1 \pm 2.3$
Observed	2	0	4	7

Table 3: Expected SM background event yields and number of events observed in data for an integrated luminosity of  $1.04 \text{ fb}^{-1}$  after the signal region requirements for the electron and muon channels. The uncertainties are a combination of the statistical and systematic uncertainties.

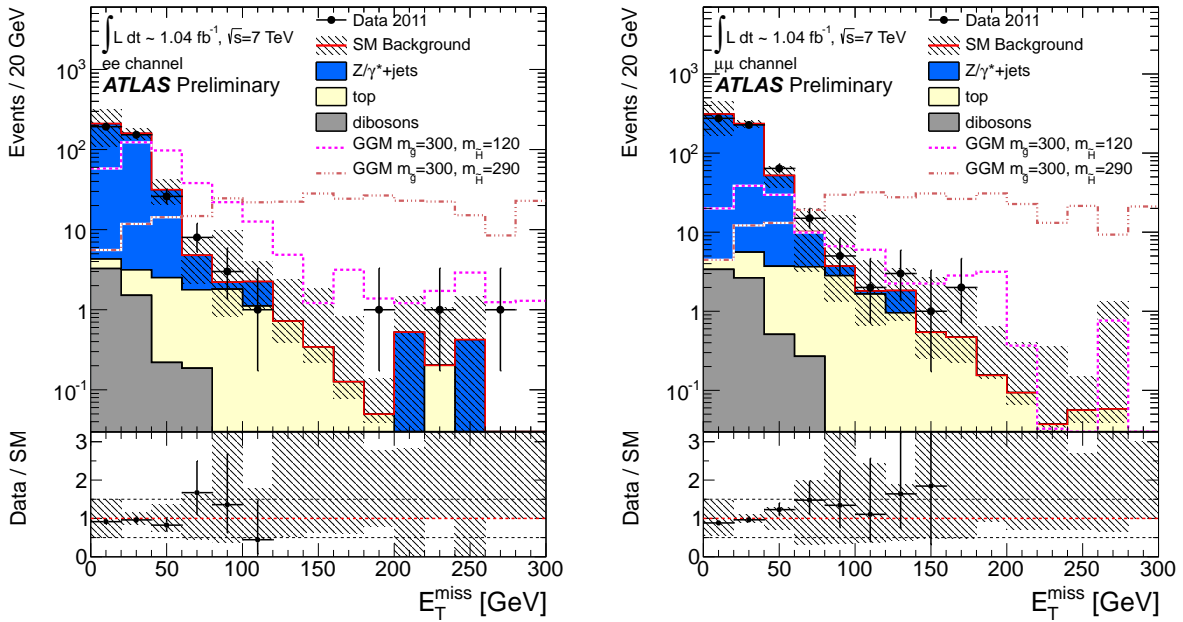


Figure 4: Distributions of  $E_T^{\text{miss}}$  for data and MC events after SR1 selection without the  $E_T^{\text{miss}}$  requirement for the  $ee$  (left) and  $\mu\mu$  (right) channels. Two GGM signal points are included. The first point was produced with  $m(\tilde{g}) = 300 \text{ GeV}$  and  $m(\tilde{H}) = 120 \text{ GeV}$ , and the second with  $m(\tilde{g}) = 300 \text{ GeV}$  and  $m(\tilde{H}) = 290 \text{ GeV}$ . The hatched grey band represents the total systematic uncertainties on the MC expectations. The plots include the overflow bin.

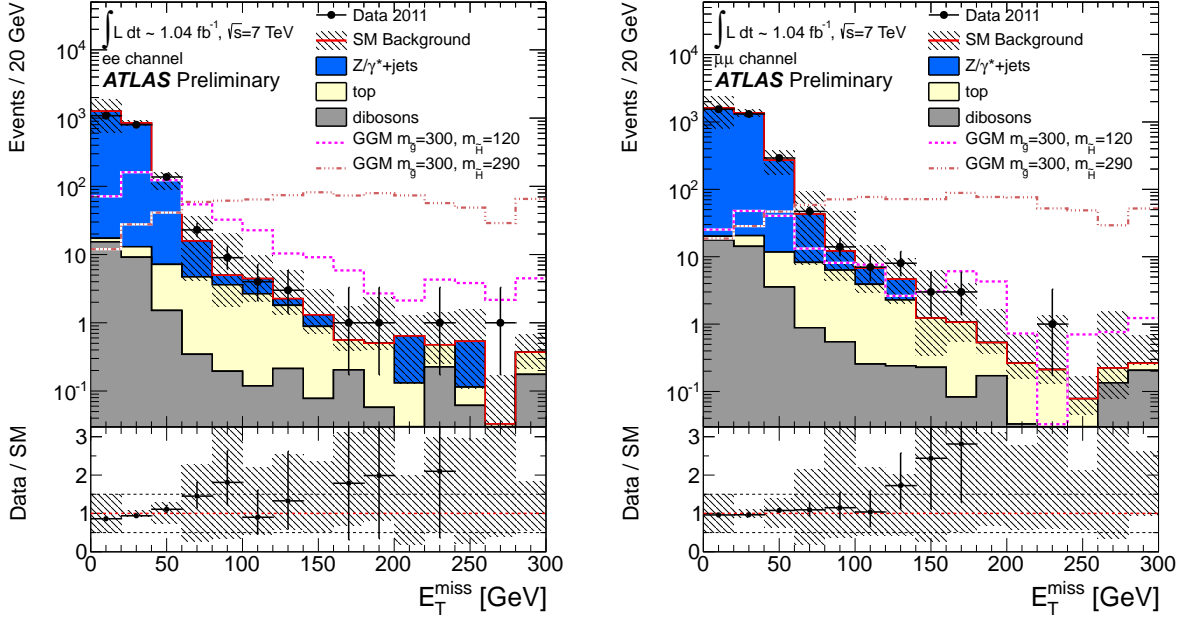


Figure 5: Distributions of  $E_T^{\text{miss}}$  for data and MC events after SR2 selection without the  $E_T^{\text{miss}}$  requirement for the  $ee$  (left) and  $\mu\mu$  (right) channels. Two GGM signal points are included. The first point was produced with  $m(\tilde{g}) = 300$  GeV and  $m(\tilde{H}) = 120$  GeV, and the second with  $m(\tilde{g}) = 300$  GeV and  $m(\tilde{H}) = 290$  GeV. The hatched grey band represents the total systematic uncertainties on the MC expectations. The plots include the overflow bin.

In the SRs, the expectation and observation agree within uncertainties. Given a lack of excess in the observed data, the results of the analysis are interpreted as 95% confidence level (CL) exclusion limits on  $m(\tilde{g})$  and  $m(\tilde{H})$  in the higgsino-like NLSP scenario defined for the GGM model grid. The expected and observed 95% CL upper limits are computed using the  $CL_s$  method combining the  $ee$  and  $\mu\mu$  channels. Systematic uncertainties are treated as nuisance parameters, and their correlations are taken into account. Limits are computed for each signal region, and the final exclusion uses the values from the signal region corresponding to the strongest expected limit.

Figure 6 shows the observed and expected 95% CL limits on  $m(\tilde{g})$  and  $m(\tilde{H})$  for the GGM models with higgsino-like NLSP considered. For higgsino masses in the range 200 – 640 GeV, gluino masses of 600 – 700 GeV are excluded at 95% CL.

## 8 Conclusions

A search for events with large  $E_T^{\text{miss}}$  and a Z boson that decays to a pair of electrons or muons has been performed using  $1.04 \text{ fb}^{-1}$  of ATLAS data collected in 2011. With no excess observed in the selected signal regions, limits on  $m(\tilde{g})$  and  $m(\tilde{H})$  have been derived in the context of GGM, when the lightest neutralino NLSP is higgsino-like. Assuming  $\tan\beta = 1.5$ ,  $M_1 = M_2 = 1$  TeV, and  $c\tau_{\text{NLSP}} < 0.1$  mm, we exclude gluino masses up to 600 – 700 GeV at 95% CL for higgsino masses in the range 200 – 640 GeV.

## References

[1] H. Miyazawa, *Prog. Theor. Phys.* **36** (6) (1966) 1266–1276.

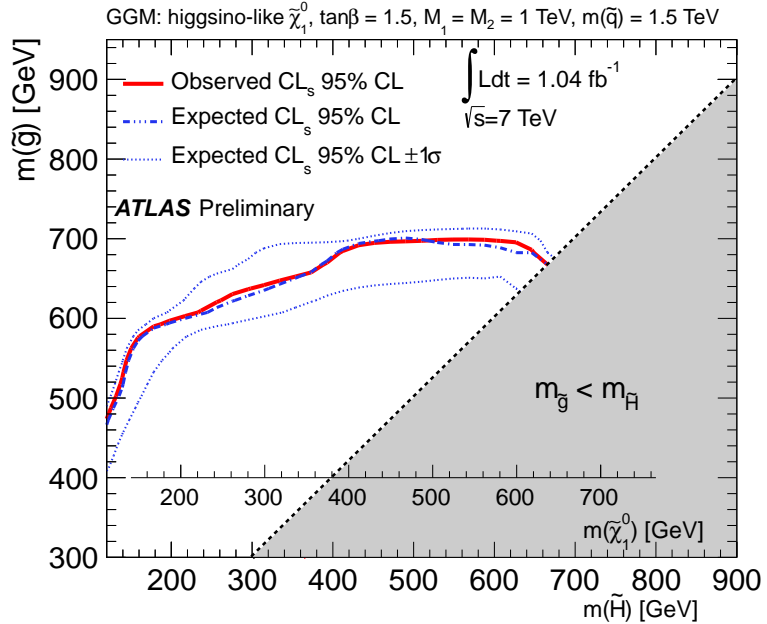


Figure 6: Expected and observed 95% CL exclusion limits on the  $m(\tilde{g})$  and  $m(\tilde{H})$  parameters for GGM models with  $\tan\beta = 1.5$ ,  $M_1 = M_2 = 1$  TeV,  $c\tau_{\text{NLSP}} < 0.1$  mm, and  $m(\tilde{q}) = 1.5$  TeV. An additional axis corresponding to  $m(\tilde{\chi}_1^0)$  is provided. The grey area indicates the region where the NLSP is the gluino, which is not considered in this analysis.

- [2] P. Ramond, [Phys. Rev. \*\*D3\*\* \(1971\) 2415–2418](#).
- [3] Y. A. Golfand and E. P. Likhtman, [JETP Lett. \*\*13\*\* \(1971\) 323–326](#).
- [4] A. Neveu and J. H. Schwarz, [Nucl. Phys. \*\*B31\*\* \(1971\) 86–112](#).
- [5] A. Neveu and J. H. Schwarz, [Phys. Rev. \*\*D4\*\* \(1971\) 1109–1111](#).
- [6] J. Gervais and B. Sakita, [Nucl. Phys. \*\*B34\*\* \(1971\) 632–639](#).
- [7] D. V. Volkov and V. P. Akulov, [Phys. Lett. \*\*B46\*\* \(1973\) 109–110](#).
- [8] J. Wess and B. Zumino, [Phys. Lett. \*\*B49\*\* \(1974\) 52](#).
- [9] J. Wess and B. Zumino, [Nucl. Phys. \*\*B70\*\* \(1974\) 39–50](#).
- [10] P. Fayet, [Phys. Lett. \*\*B64\*\* \(1976\) 159](#).
- [11] P. Fayet, [Phys. Lett. \*\*B69\*\* \(1977\) 489](#).
- [12] G. R. Farrar and P. Fayet, [Phys. Lett. \*\*B76\*\* \(1978\) 575–579](#).
- [13] P. Fayet, [Phys. Lett. \*\*B84\*\* \(1979\) 416](#).
- [14] S. Dimopoulos and H. Georgi, [Nucl. Phys. \*\*B193\*\* \(1981\) 150](#).
- [15] M. Dine and W. Fischler, [Phys. Lett. \*\*B110\*\* \(1982\) 227](#).
- [16] L. Alvarez-Gaume et al., [Nucl. Phys. \*\*B207\*\* \(1982\) 96](#).

- [17] C. R. Nappi and B. A. Ovrut, *Phys. Lett.* **B113** (1982) 175.
- [18] M. Dine and A. E. Nelson, *Phys. Rev.* **D48** (1993) 1277–1287.
- [19] M. Dine et al., *Phys. Rev.* **D51** (1995) 1362–1370.
- [20] M. Dine et al., *Phys. Rev.* **D53** (1996) 2658–2669.
- [21] CDF Collaboration, T. Aaltonen et al., *Phys. Rev. Lett.* **104** (2010) 011801.
- [22] D0 Collaboration, V. M. Abazov et al., *Phys. Rev. Lett.* **105** (2010) 221802.
- [23] P. Meade et al., *Prog. Theor. Phys. Suppl.* **177** (2009) 143–158.
- [24] M. Buican et al., *JHEP* **03** (2009) 016.
- [25] ATLAS Collaboration, *Phys. Lett.* **B710** (2012) 519–537.
- [26] CMS Collaboration, *Phys. Rev. Lett.* **106** (2011) 211802.
- [27] CMS Collaboration, *JHEP* **1106** (2011) 093.
- [28] P. Meade et al., *JHEP* **1005** (2010) 105.
- [29] J. T. Ruderman and D. Shih, [arXiv:1103.6083 \[hep-ph\]](https://arxiv.org/abs/1103.6083) (2011).
- [30] ATLAS Collaboration, *JINST* **3** (2008) S08003.
- [31] A. Djouadi et al., *Comput. Phys. Commun.* **176** (2007) 426–455.
- [32] M. Muhlleitner et al., *Comput. Phys. Commun.* **168** (2005) 46–70.
- [33] T. Sjostrand et al., *JHEP* **05** (2006) 026.
- [34] A. Sherstnev and R. Thorne, *Eur.Phys.J.* **C55** (2008) 553–575.
- [35] W. Beenakker et al., [arXiv:hep-ph/9611232](https://arxiv.org/abs/hep-ph/9611232) (1996).
- [36] D. Stump et al., *JHEP* **10** (2003) 046.
- [37] S. Frixione and B. R. Webber, [arXiv:hep-ph/0601192 \[hep-ph\]](https://arxiv.org/abs/hep-ph/0601192) (2006).
- [38] P. M. Nadolsky et al., *Phys. Rev.* **D78** (2008) 013004.
- [39] S. Frixione et al., *JHEP* **11** (2007) 070.
- [40] B. P. Kersevan and E. Richter-Was, [arXiv:hep-ph/0405247](https://arxiv.org/abs/hep-ph/0405247) (2004).
- [41] M. L. Mangano et al., *JHEP* **0307** (2003) 001.
- [42] J. Pumplin et al., *JHEP* **0207** (2002) 012.
- [43] G. Corcella et al., *JHEP* **01** (2001) 010.
- [44] J. Butterworth et al., *Z.Phys.* **C72** (1996) 637–646.
- [45] GEANT4 Collaboration, *Nucl. Instrum. Meth.* **A506** (2003) 250–303.
- [46] ATLAS Collaboration, *Eur. Phys. J.* **C70** (2010) 823–874.

- [47] ATLAS Collaboration, *Eur. Phys. J.* **C71** (2011) 1630.
- [48] M. Cacciari et al., *JHEP* **0804** (2008) 063.
- [49] ATLAS Collaboration, *Eur. Phys. J.* **C72** (2012) 1909.
- [50] ATLAS Collaboration, ATLAS-CONF-2011-063 (2011).
- [51] ATLAS Collaboration, *Phys. Rev.* **D83** (2011) 052005.
- [52] ATLAS Collaboration, *Eur. Phys. J.* **C72** (2012) 1844.